ACS APPLIED MATERIALS & INTERFACES

www.acsami.org

Research Article

Two-Dimensional-Like Phonons in Three-Dimensional-Structured Rhombohedral GeSe-Based Compounds with Excellent Thermoelectric Performance

Jingjing Cui,[†] Chenghao Xie,[†] Weiwei Hu, Hao Luo, Qicai Mei, Songlin Li, Weibin Xu, Zhibin Gao, Jinsong Wu, Qingjie Zhang, Xinfeng Tang, and Gangjian Tan*

Cite This: *ACS Appl. Mater. Interfaces* 2024, 16, 39656−39663

Read Online

ACCESS | Metrics & More | Article Recommendations | Supporting Information

ABSTRACT: The coupling of charge and phonon transport in solids is a long-standing issue for thermoelectric performance enhancement. Herein, two new narrow-gap semiconductors with the same chemical formula of $GeSe_{0.65}Te_{0.35}$ (GST) are rationally designed and synthesized: one with a layered hexagonal structure (H-GST) and the other with a non-layered rhombohedral structure (R-GST). Thanks to the three-dimensional (3D) network structure, R-GST possesses a significantly larger weighted mobility than H-GST. Surprisingly, 3D-structured R-GST displays an extremely low lattice thermal conductivity of ∼0.5 W m^{-1} K^{-1} at 523 K, which is comparable to that of layered H-GST. The two-dimensional (2D)-like phonon transport in R-GST stems from the unique off-centering Ge atoms that induce ferroelectric instability, yielding soft polar phonons, as demonstrated by the Boson peak detected by the low-temperature specific heat and calculated phonon spectra. Furthermore, 1 mol % doping of Sb is utilized to successfully suppress the undesired phase transition of R-GST toward H-GST at elevated temperatures. Consequently, a peak ZT of 1.1 at 623 K is attained in the rhombohedral $Ge_{0.99}Sb_{0.01}Se_{0.65}Te_{0.35}$ sample, which is 1 order of magnitude larger than that of GeSe. This work demonstrates the feasibility of exploring high-performance thermoelectric materials with decoupled charge and phonon transport in off-centering compounds.

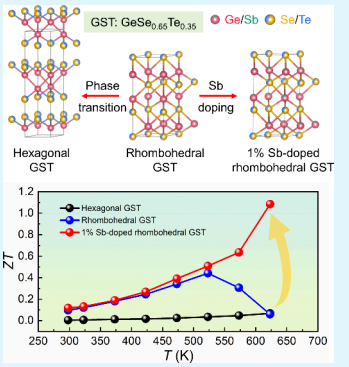

KEYWORDS: *2D phonons, GeSe, thermoelectric, weighted mobility, thermal conductivity*

1. INTRODUCTION

About two-thirds of the worldwide energy consumption is wasted as heat and can possibly be recovered by use of thermoelectric devices.[1−4] At a given temperature gradient, thermoelectric conversion efficiency is related to the dimensionless figure of merit of the materials, $ZT = S^2\sigma T/\kappa_{tot}$, where S, σ, T, and κ_{tot} denote the Seebeck coefficient, electrical conductivity, absolute temperature, and total thermal conductivity, respectively.[5] Usually, the term $S^2\sigma$ reflects the electrical properties of thermoelectric materials and is measured by the weighted mobility $\mu_w \approx \mu_H(m^*_{DOS}/m_e)^{3/2}$.[6] Here, μ_H is the Hall mobility of charge carriers, m^*_{DOS} is the density of states effective mass, and m_e is the inertial mass of free electrons. κ_{tot}, on the other hand, is a sum of the lattice thermal conductivity (κ_{lat}) and electronic thermal conductivity (κ_{ele}). The strong coupling between these charge and phonon transport parameters complicates the optimization of ZT in thermoelectric materials.[7]

Normally, two-dimensional (2D) materials exhibit intrinsically low values of κ_{lat} because phonons are strongly impeded when they propagate through the interlayers.[8,9] Typical examples include $Bi_{2-x}Sb_xTe_3$,[10,11] BiCuSeO,[12−14] SnSe,[15,16] $Bi_m(Bi_2Se_3)_n$,[17,18] etc. Unfortunately, in most cases, the 2D materials also heavily scatter charge carriers for the same reason.[19] On the contrary, the three-dimensional (3D)-structured non-layered compounds usually display high μ_w but, meanwhile, larger κ_{lat} than 2D materials.[20] There are only very few exemptions that large μ_w and low κ_{lat} are simultaneously recorded in one single material;[21,22] i.e., charge and phonon transports are decoupled.

2D orthorhombic GeSe has been theoretically predicted to possess an excellent ZT of 2.5 at 800 K because of its exceptionally low κ_{lat}.[23] However, experimentally, the potential of GeSe as an advanced thermoelectric material was not fully realized. For one thing, GeSe is hardly doped to populate sufficient charge carriers;[24,25] for another, the layered structure of GeSe sacrifices μ_w, leading to poor PF. Recent studies demonstrate considerably improved thermoelectric performance of GeSe by modifying its crystal structure.[26−31] For instance, through alloying with $AgSbSe_2$, 2D GeSe transforms into the 3D rhombohedral structure.[32] The resultant Ge-

Received: May 17, 2024
Revised: July 10, 2024
Accepted: July 12, 2024
Published: July 20, 2024

$(AgSb)_xSe_{1+2x}$ samples show much higher values of μ_w. In addition, the new compound is proven to be heavily self-doped with a hole concentration on the order of 10^{20} cm^{-3} at room temperature, far larger than that ($\sim 10^{16}$ cm^{-3}) of pristine GeSe.[25] More importantly, low κ_{lat} of GeSe is well-reserved in rhombohedral $Ge(AgSb)_xSe_{1+2x}$, leading to a maximum ZT of ~0.86 at 710 K in the $x = 0.2$ sample. Similar results are found when GeSe is alloyed with $AgSbTe_2$,[33] $AgBiSe_2$,[34] $AgInTe_2$,[35] $AgBiTe_2$,[36] and $MnCdTe_2$.[37]

Despite the above-mentioned progress, the origin of low κ_{lat} in rhombohedral GeSe remains unclear. Particularly, because heavy alloying is necessary to stabilize the rhombohedral structure of GeSe, it is natural to ask whether atom disorder contributes to its high thermal resistance. To answer the question, in this work, by a subtle design of the synthesis condition (detailed in the Experimental Section) according to the GeSe−GeTe pseudo-binary phase diagram,[38,39] two different narrow gap semiconductors with the same chemical composition of $GeSe_{0.65}Te_{0.35}$ (GST) have been successfully prepared (see their powder X-ray diffraction patterns in Figure S1 of the Supporting Information and densities listed in Table S1 of the Supporting Information): one adopts the 3D-structured rhombohedral structure (denoted as R-GST) with a trace second phase of *Pnma* GeSe, and the other crystallizes in a 2D-layered hexagonal structure (denoted as H-GST) separated by the van der Waals gap (Figure 1a). Interestingly, in R-GST, the octahedron of $[Ge(Se/Te)_6]$ contains three longer bonds of 3.077 Å and three much shorter bonds of 2.732 Å, implying that Ge atoms are apparently displaced from the octahedron center. Such an off-centering behavior of Ge (supported by the Rietveld refinement structural parameters in Table S2 of the Supporting Information) stems from the strong thermodynamic driving force of the $4s^2$ lone pair electrons to stereochemically express itself and might give rise to robust ferroelectricity, as seen in $BaTiO_3$[40,41] and GeTe.[42,43] Indeed, herringbone-like ferroelectric domains are clearly observed in R-GST under transmission electron microscopy (TEM) (Figure S2 of the Supporting Information).

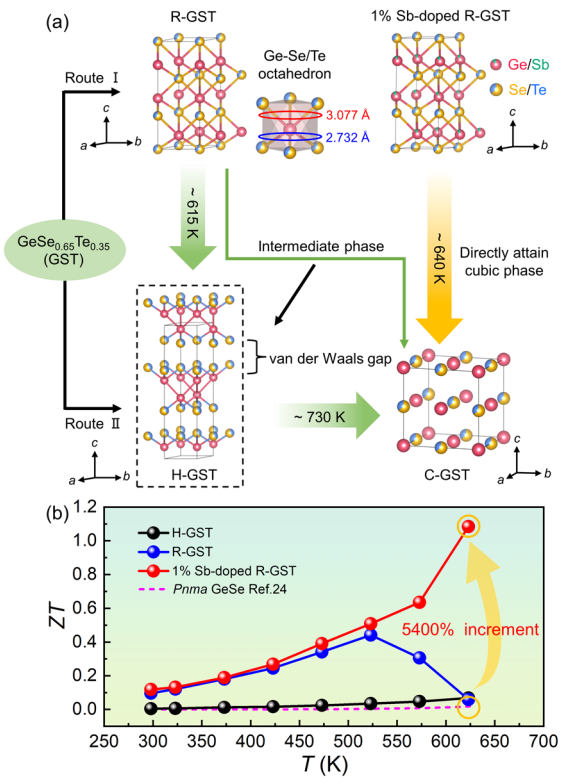

Figure 1. (a) Crystal structures of R-GST, H-GST, C-GST, and 1% Sb-doped R-GST and their evolution with the temperature. $[Ge(Se/Te)_6]$ octahedron and the bond lengths are illustrated. The synthesis routes I and II of GST are described in the Experimental Section. (b) Comparison of ZT values for R-GST, H-GST, and 1% Sb-doped R-GST in this work and GeSe, which is reproduced with permission from ref 24. Copyright 2016 Elsevier.

2. EXPERIMENTAL SECTION

2.1. Material Synthesis. High-purity (>99.99%) elements Ge, Se, Te, and Sb were weighted in a stochiometric ratio and sealed in quartz tubes under vacuum. With 8 h of melting at 1173 K and subsequent water quenching (route I), samples were crystallized in the rhombohedral phase, while the hexagonal crystal was synthesized with an additional 12 h of annealing at 623 K (route II). The resulting ingots were ground into fine powders and consolidated by spark plasma sintering under 60 MPa pressure at 773 K for 10 min in high vacuum.

2.2. Phase and Microstructure Characterization. The phase structure was characterized by powder X-ray diffraction (XRD, Epyrean, PANalytical). Temperature-dependent powder XRD was carried for R-GST and 1% Sb-doped R-GST under a N_2 atmosphere (D/max 2400, Riguka). Differential scanning calorimetry (DSC) curves were carried out on Q20 (TA Instrument) under a heating rate of 5 K/min.

2.3. Thermoelectric Property Measurements. The electrical resistivity and Seebeck coefficient were measured with a Cryoall CTA-3 instrument system. The thermal diffusivity (D) was examined by the laser flash method (LFA-457, Netzsch), and the thermal conductivity κ_{tot} is obtained by $\kappa_{tot} = DC_p\rho$, where C_p is the heat capacity derived from the empirical Dulong−Petit law and ρ is the density estimated by the Archimedes method. The thermal diffusivity was measured along the same direction as the electrical transport for both H-GST and R-GST. Considering the isotropy characteristic exhibited by the rhombohedral structure, we measured the electrical properties perpendicular to the sintering direction and the thermal diffusivity parallel to the sintering direction for 1% Sb-doped R-GST. Cryogenic C_p was tested in the physical property measurement system (PPMS-9, Quantum Design) from 2 to 300 K. The carrier concentration (p_H) and Hall mobility (μ_H) were measured on the Hall system (Lakeshore 8404).

2.4. Computational Details. Phonon dispersions and band structures were performed by density functional theory (DFT) calculations. All of the calculations were performed using the generalized gradient approximation with the Perdew−Burke−Ernzerhof (PBE) functional[44] for the exchange−correlation functional and projector augmented wave potentials as implemented in Vienna *Ab initio* Simulation Package (VASP).[45] We constructed several $Ge_8Te_3Se_5$ crystal cells belonging to the $R3m$ and $P6_3mc$ space groups and calculated the energies, respectively. The crystal structure with the lowest energy was selected for subsequent phonon calculations, for which $2 \times 2 \times 2$ supercells were employed to capture the phonon dispersions. The k paths of Γ−M−K−Γ−A−L−H−A|L−M|H−K for H-GST and Γ−T−H_2|H_0−L−Γ−S_0|S_2−F−Γ for R-GST were adopted. A total of 100 k points were scattered between each high-symmetry point.

3. RESULTS AND DISCUSSION

A combinational study of temperature-variant XRD and DSC suggests that R-GST undergoes a two-step phase transition upon warming: transformation into (i) H-GST at ~615 K and then (ii) cubic rock salt structure (C-GST, space group of $Fm\bar{3}m$) at ~730 K; see the flow guided by the green arrow in Figure 1a. Specifically, as shown in Figure 2a, R-GST retains its

https://doi.org/10.1021/acsami.4c08186
ACS Appl. Mater. Interfaces 2024, 16, 39656−39663

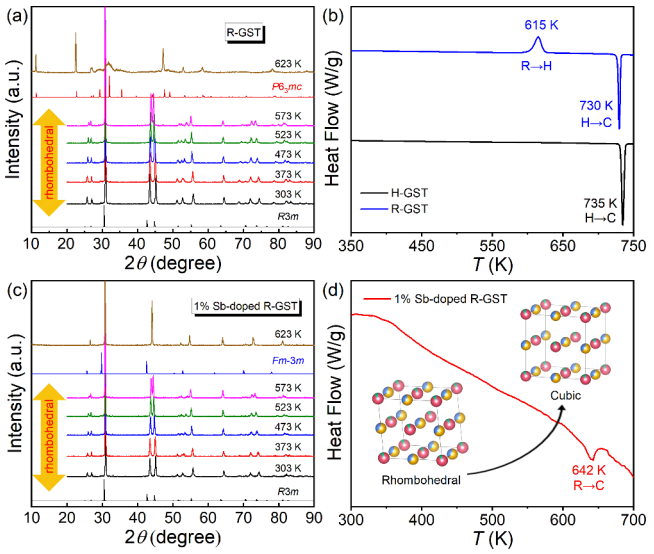

Figure 2. *In situ* XRD studies on (a) R-GST and (c) 1% Sb-doped R-GST. The DSC curves of (b) H-GST and R-GST and (d) 1% Sb-doped R-GST. The inset of panel d illustrates the crystal structure of 1% Sb-doped R-GST before and after phase transition.

rhombohedral structure (space group of *R*3*m*) with small peaks of H-GST (space group of $P6_3mc$) when $T \leq 573$ K. However, at T = 623 K, R-GST has already completely transformed into H-GST. Correspondingly, there is an exothermic peak at 615 K in the DSC curve of R-GST (Figure 2b), which is unambiguously attributed to the rhombohedral to hexagonal (R → H) phase transition. We also note a strong endothermic peak at 730 K (735 K) in the DSC curve of R-GST (H-GST). Because Se vapor easily contaminates the Pt heater at a high temperature, we are not able to heat the samples exceeding 650 K during the *in situ* XRD measurement. Therefore, the X-ray technique is unlikely to be employed for the direct determination of phase evolution above 700 K. However, the endothermic peak at ~730 K is most likely related to the hexagonal to cubic (H → C) phase transition of GST, as concluded from the GeSe−GeTe pseudo-binary phase diagram.

Sb (1 mol %) doping in R-GST (1% Sb-doped R-GST) efficiently eliminates the R → H phase transition. As illustrated in Figure 2c, 1% Sb-doped R-GST has a consistent rhombohedral structure until 623 K, where it becomes cubic. The corresponding DSC curve (Figure 2d) also reveals only one broadened endothermic peak at ~642 K, which is ascribed to the rhombohedral to cubic (R → C) phase transition.

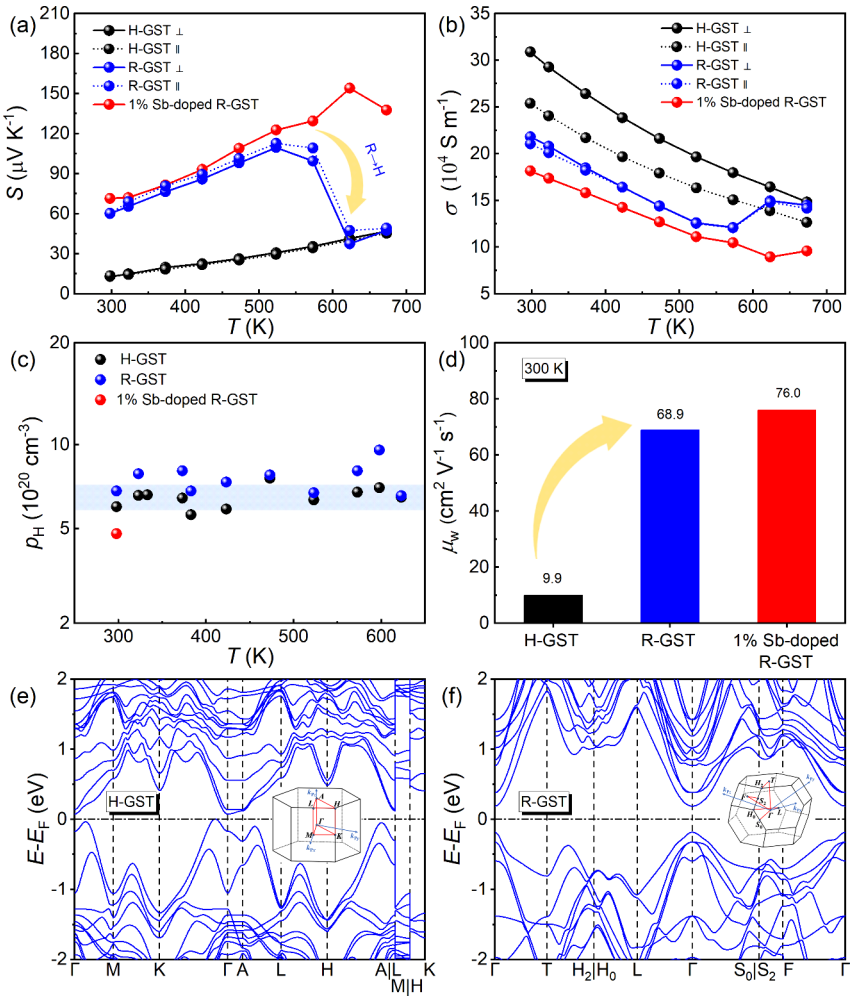

Figure 3. Temperature-dependent (a) Seebeck coefficients and (b) electrical conductivities for H-GST, R-GST, and 1% Sb-doped R-GST. Comparison of (c) temperature-dependent p_H and (d) room-temperature values of μ_w. The theoretical electronic band structures of (e) H-GST and (f) R-GST. Insets of panels e and f illustrate the first Brillouin zone of the two compounds.

https://doi.org/10.1021/acsami.4c08186
ACS Appl. Mater. Interfaces 2024, 16, 39656−39663

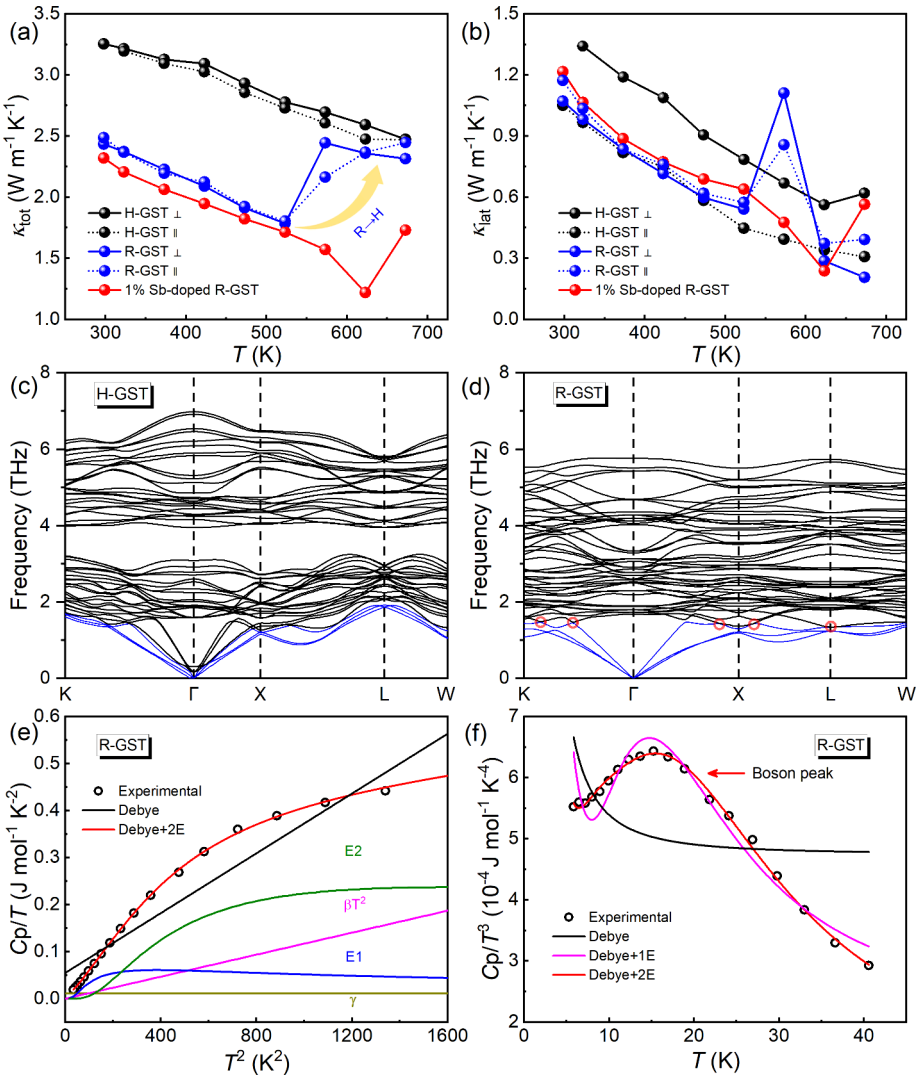

Figure 4. (a) Total and (b) lattice thermal conductivity as a function of the temperature for H-GST, R-GST, and 1% Sb-doped R-GST samples. The calculated phonon spectra of (c) H-GST and (d) R-GST. The red circles in panel d demonstrate the avoided crossing of the low-frequency optical modes with the acoustic modes. (e) C_p/T versus T^2 in the temperature range of 5−40 K for R-GST. The black and red solid lines are calculated by a simple Debye and combined Debye−2Einstein model, respectively. The individual contributions of electronic (γ), lattice (βT^2), and two Einstein resonators (E1 and E2) are also illustrated. (f) C_p/T^3 as a function of T for R-GST. The black, pink, and red solid lines are fitted by simple Debye, Debye−1Einstein (Debye + 1E), and Debye−2Einstein (Debye + 2E) models, respectively. An obvious Boson peak is present by the red arrow in the plot.

As displayed in Figure 1b, the maximum ZT (perpendicular to the sintering pressure direction, unless otherwise noted) of 2D-layered H-GST is ∼0.1 at 623 K, only slightly larger than that of pristine GeSe. By comparison, R-GST shows significantly boosted ZT values below 523 K because of its 2D-like phonon transport in the 3D non-layered structure (which will be detailed in the following section). However, the thermoelectric performance of R-GST quickly degrades once the R → H phase transition occurs. The adverse R → H phase transition vanishes in the 1% Sb-doped R-GST sample, leading to the ZT value continuously ramping to 1.1 at 623 K and outperforming many other rhombohedral GeSe-based compounds reported thus far[29,33,37,46,47] (Figure S4 of the Supporting Information).

The temperature-dependent Seebeck coefficients and electrical conductivities of R-GST, H-GST, and 1% Sb-doped R-GST are displayed in panels a and b of Figure 3, respectively. For R-GST and H-GST, the thermoelectric transport data have been collected both perpendicular (⊥) and parallel (∥) to the sintering pressure direction. Both the values of σ and S are practically isotropic in R-GST, which is consistent with its 3D non-layered structure. For this reason, we only provide the σ and S data of 1% Sb-doped R-GST measured perpendicular to the sintering direction. In contrast, S is identical but σ differs a lot in the two directions of H-GST, characteristic of 2D-layered materials.

The Seebeck coefficients (electrical conductivities) of R-GST are significantly larger (slightly lower) than those of H-GST below 523 K, but they suddenly drop (increase) beyond that temperature because of the ongoing R → H phase transition and finally approach those of H-GST at $T \geq 623$ K when the transition process is finished. Such abnormal changes of S and σ in the temperature interval of 523−623 K, however, are absent in 1% Sb-doped R-GST as a result of the elimination of the R → H phase transition. Instead, S (σ) keeps going up (down) until 623 K, where the R → C phase transition starts

https://doi.org/10.1021/acsami.4c08186
ACS Appl. Mater. Interfaces 2024, 16, 39656−39663

to take effect. The similar trends can be seen in power factors (*PF*) for as-sintered samples (Figure S3 of the Supporting Information).

Figure 3c depicts the hole concentration (p_H) as a function of the temperature for R-GST, H-GST, and 1% Sb-doped R-GST. p_H is similar and basically temperature-independent for all three samples, scattering around 6.6 (±10%) × 10^{20} cm^{-3} from 300 to 623 K (they are heavily self-doped because of the spontaneously formed Ge vacancies), as highlighted by the shadowed rectangle. Therefore, it is plausible that R-GST and 1% Sb-doped R-GST resemble each other in *S* below 523 K. Nonetheless, R-GST displays considerably larger Seebeck coefficients than H-GST before the R → H phase transition, despite their similar p_H. Assuming that a single parabolic band dominated charge transfer and acoustic phonons dominated carrier scattering,[48] *S* is expressed as

$$S = \frac{8\pi^2 k_B^2 T}{3eh^2} m^*_{DOS} \left(\frac{\pi}{3p_H}\right)^{2/3} \quad (1)$$

where *e*, *h*, and k_B represent the electronic charge, Planck constant, and Boltzmann constant, respectively. The derived value of m^*_{DOS} from the above equation is 2.34m_e for R-GST, which is much larger than that (0.46m_e) of H-GST.

The electronic band structures of H-GST and R-GST are computed from first principles within DFT. To simplify the calculations, $Ge_8Se_5Te_3$ supercells are used as the approximation of $GeSe_{0.65}Te_{0.35}$ and are fully relaxed in the context of *R*3*m* and $P6_3mc$ space groups. As illustrated in panels e and f of Figure 3, both H-GST and R-GST are narrow gap semiconductors. Specifically, H-GST is an indirect band gap (E_g ∼ 0.07 eV) semiconductor, with the valence band maxima (VBM) being slightly off the Γ point. On the other hand, R-GST features a much larger direct E_g of 0.37 eV separated by the VBM and conduction band minima (CBM) both located at the Γ point. For most semiconducting thermoelectric materials, the band dispersion satisfies the Kane band model[49]

$$\frac{\hbar^2 k^2}{2m^*_b} = E\left(1 + \frac{E}{E_g}\right) \quad (2)$$

where $\hbar$ is the reduced Planck constant, *k* is the crystal momentum, *E* is the energy of electron states, and m^*_b is the band effective mass that relates to m^*_{DOS} through the equation[50]

$$m^*_{DOS} = (N_V)^{2/3} m^*_b \quad (3)$$

where N_V is the effective band degeneracy and approximates 1 for both compounds at their VBM of the Γ point (see the first Brillouin zone illustrated in the insets of panels e and f of Figure 3). From eqs 2 and 3, it can be concluded that the larger E_g in R-GST should largely account for its larger values of m^*_{DOS} with respect to H-GST.

Although R-GST has a 5 times larger m^*_{DOS} than H-GST, their Hall mobilities differ insignificantly. Specifically, at room temperature, the values of μ_H are ∼31.8 and ∼26.2 $cm^2\ V^{-1}\ s^{-1}$ for H-GST perpendicular and parallel to the sintering directions, respectively; for comparison, μ_H is only ∼25−40% lower for R-GST, namely, ∼19.2 $cm^2\ V^{-1}\ s^{-1}$ in both directions. Despite the Hall mobility being a good estimate (within 10−20%) for the drift mobility of charge carriers in most cases, the weighted mobility is actually a better descriptor of the inherent transport property than the Hall mobility because it is more independent of the charge carrier concentration and has a more consistent temperature dependence.[51] Figure 3d compares the values of μ_w (perpendicular to the sintering direction) for the three samples investigated in this study. Owing to the 3D non-layered structure, R-GST and 1% Sb-doped R-GST display considerably larger values (68.9 and 76.0 $cm^2\ V^{-1}\ s^{-1}$, respectively) than 2D-layered H-GST (9.9 $cm^2\ V^{-1}\ s^{-1}$).

The total and lattice thermal conductivities of H-GST, R-GST, and 1% Sb-doped R-GST are depicted in panels a and b of Figure 4, respectively. Similar to the trends found in electrical transport properties, there is an abrupt rise of κ_{tot} starting from 523 K for R-GST as a result of the R → H phase transition, and this anomaly vanishes in 1% Sb-doped R-GST. Moreover, κ_{lat} shows strong anisotropy for H-GST but not for the two rhombohedral compounds. Surprisingly, 3D non-layered R-GST displays comparable or even lower κ_{lat} than 2D H-GST. At 673 K, an exceptionally low κ_{lat} of 0.2 $W\ m^{-1}\ K^{-1}$ is attained in R-GST perpendicular to the sintering pressure direction. As a comparison, κ_{lat} is 0.6 $W\ m^{-1}\ K^{-1}$ for 2D H-GST measured along the same direction.

To understand the origin of ultralow κ_{lat}, the phonon dispersions of H-GST and R-GST were calculated on the basis of the first-principles theory, and the results are displayed in panels c and d of Figure 4, respectively. Both hexagonal and rhombohedral GST are supposed to be dynamically stable because no imaginary frequency appears in their phonon spectrum. An apparent frequency gap (between 3 and 4 THz), however, is observed in the phonon spectrum of H-GST, which likely arises from its 2D crystal structure. In addition, the cutoff frequency of acoustic modes of R-GST is suppressed below 1.5 THz as a result of the avoided crossing (highlighted by the red circles) of the low-frequency optical modes with the acoustic modes. This value is comparable to ∼1.6 THz for SnSe[52] and ∼1.5 THz for PbTe[53] but much lower than 1.9 THz for H-GST. The avoided crossing between the optical and acoustic modes has generally been considered as a sign of phonon coupling and a hallmark of low thermal conductivity.[54−56]

An experimental examination of the phonon coupling can be carried out by detecting the Boson peak in the specific heat (C_p) measurement. Considering only the contribution of long-wave phonons to specific heat, the traditional Debye model can well describe the specific heat behavior of many materials at low temperatures.[57−59] However, as shown in Figure 4e, the simple Debye model fails to describe the experimental results of R-GST, indicating that the acoustic phonon modes alone are insufficient to explain the observed specific heat. Therefore, multiple Einstein oscillator modes must be considered. Indeed, the plot of C_p/T versus T^2 for R-GST in the temperature range of 5−40 K can be well-fitted when employing the Debye−2Einstein model expressed as[60]

$$\frac{C_p}{T} = \gamma + bT^2 + \sum_n A_n(\Theta_{En})^2 (T^2)^{-3/2} \frac{e^{\Theta_{En}/T}}{(e^{\Theta_{En}/T} - 1)^2} \quad (4)$$

In eq 4, γ and bT^2 represent the contribution of electrons and lattice to C_p, respectively, the integral term stands for Einstein resonator contribution, where *n* is the number of Einstein resonator modes, A_n is the prefactor of the *n*th Einstein resonator mode, and Θ_{En} is the characteristic Einstein temperature of the *n*th Einstein mode. The fitting of low-

https://doi.org/10.1021/acsami.4c08186
ACS Appl. Mater. Interfaces 2024, 16, 39656−39663

temperature specific heat data of R-GST provides evidence for the existence of at least two low-lying Einstein resonator modes, and the derived Einstein temperatures from the fitting (see Table S3 of the Supporting Information) are Θ_{E1} = 53.8 K (1.12 THz) and Θ_{E2} = 109.4 K (2.28 THz). The Einstein mode of Θ_{E1} is in line with the avoided crossing frequency (1.34 THz) of acoustic modes in the phonon dispersion of R-GST (Figure 4d), which verifies the strong phonon coupling in the material.[61]

Using the Debye−2Einstein model to fit the low-temperature C_p data of R-GST, an extreme peak emerges between 10 and 20 K in the C_p/T^3-T plot, which is referred to as the Boson peak (Figure 4f). The Boson peak is usually detected in materials with intrinsically low thermal conductivity, and its possible origin could be (i) intrinsic disorder in the harmonic force constants (frequently seen in amorphous alloys)[62] and (ii) strong coupling between acoustic phonons and low-frequency optical phonons,[63] which is the case in the present study. The preceding structural diagram (Figure 1a) and TEM analysis (Figure S2 of the Supporting Information) demonstrate the off-centering Ge atoms and associated ferroelectric domains in R-GST. The resultant ferroelectric lattice instability induces soft low-lying polar phonons that interfere strongly with the heat-carrying acoustic phonons and help achieve 2D-like phonon transport in 3D non-layered R-GST.

4. CONCLUSION

In this study, by rationally controlling the synthesis conditions, we have successfully obtained two narrow gap semiconductors with the same chemical composition of $GeSe_{0.65}Te_{0.35}$: one with a 2D-layered hexagonal structure and the other with a 3D non-layered rhombohedral structure. As expected, the 3D network of rhombohedral-structured GST endows it with a superior weighted mobility compared to 2D-layered H-GST. However, the lattice thermal conductivity of R-GST is extremely low and resembles that of 2D-layered H-GST, which is beyond our expectation. The existence of low-lying optical phonon modes and the strong coupling with acoustic phonon modes in R-GST is confirmed by the Boson peak detected by the low-temperature specific heat and calculated phonon spectra, derived from the off-centering Ge atoms and the resultant ferroelectric lattice instability. The 2D-like thermal conductance in 3D-structured R-GST represents a good example of decoupling charge and phonon transport in solid crystalline materials. A minute Sb doping (1 mol %) is proven to effectively inhibit the adverse R → H phase transition of R-GST at an elevated temperature and yields a maximum value of ∼1.1 at 623 K, rendering it one of the best performing GeSe-based thermoelectric materials.

■ ASSOCIATED CONTENT

Supporting Information

The Supporting Information is available free of charge at https://pubs.acs.org/doi/10.1021/acsami.4c08186.

XRD patterns (Figure S1), TEM images (Figure S2), temperature-dependent power factors (Figure S3), comparison of maximum ZT values to relevant reports (Figure S4), room-temperature densities for sintered samples (Table S1), structural parameters of Rietveld refinement for R-GST (Table S2), and fitting parameters of the low-temperature heat capacity data for R-GST by the Debye−Einstein model (Table S3) (PDF)

■ AUTHOR INFORMATION

Corresponding Author

Gangjian Tan − *State Key Laboratory of Advanced Technology for Materials Synthesis and Processing, Wuhan University of Technology, Wuhan, Hubei 430070, People's Republic of China;* orcid.org/0000-0002-9087-4048; Email: gtan@whut.edu.cn

Authors

Jingjing Cui − *State Key Laboratory of Advanced Technology for Materials Synthesis and Processing and International School of Materials Science and Engineering, Wuhan University of Technology, Wuhan, Hubei 430070, People's Republic of China*

Chenghao Xie − *State Key Laboratory of Advanced Technology for Materials Synthesis and Processing and International School of Materials Science and Engineering, Wuhan University of Technology, Wuhan, Hubei 430070, People's Republic of China*

Weiwei Hu − *State Key Laboratory of Advanced Technology for Materials Synthesis and Processing, Wuhan University of Technology, Wuhan, Hubei 430070, People's Republic of China*

Hao Luo − *State Key Laboratory of Advanced Technology for Materials Synthesis and Processing and Nanostructure Research Center, Wuhan University of Technology, Wuhan, Hubei 430070, People's Republic of China*

Qicai Mei − *State Key Laboratory of Advanced Technology for Materials Synthesis and Processing, Wuhan University of Technology, Wuhan, Hubei 430070, People's Republic of China*

Songlin Li − *State Key Laboratory of Advanced Technology for Materials Synthesis and Processing, Wuhan University of Technology, Wuhan, Hubei 430070, People's Republic of China*

Weibin Xu − *State Key Laboratory of Advanced Technology for Materials Synthesis and Processing, Wuhan University of Technology, Wuhan, Hubei 430070, People's Republic of China*

Zhibin Gao − *State Key Laboratory for Mechanical Behavior of Materials, School of Materials Science and Engineering, Xi'an Jiaotong University, Xi'an, Shaanxi 710049, People's Republic of China;* orcid.org/0000-0002-6843-381X

Jinsong Wu − *State Key Laboratory of Advanced Technology for Materials Synthesis and Processing and Nanostructure Research Center, Wuhan University of Technology, Wuhan, Hubei 430070, People's Republic of China;* orcid.org/0000-0002-7305-7927

Qingjie Zhang − *State Key Laboratory of Advanced Technology for Materials Synthesis and Processing, Wuhan University of Technology, Wuhan, Hubei 430070, People's Republic of China*

Xinfeng Tang − *State Key Laboratory of Advanced Technology for Materials Synthesis and Processing, Wuhan University of Technology, Wuhan, Hubei 430070, People's Republic of China;* orcid.org/0000-0002-0715-5529

Complete contact information is available at: https://pubs.acs.org/10.1021/acsami.4c08186

Author Contributions

†Jingjing Cui and Chenghao Xie contributed equally to this work.

https://doi.org/10.1021/acsami.4c08186
ACS Appl. Mater. Interfaces 2024, 16, 39656−39663

Notes

The authors declare no competing financial interest.

■ ACKNOWLEDGMENTS

The authors acknowledge the financial support from the National Natural Science Foundation of China (Grants 52371235 and 52171221) and the National Key Research and Development Program of China (Grant 2019YFA0704900).

■ REFERENCES

(1) Tang, X.; Li, Z.; Liu, W.; Zhang, Q.; Uher, C. A comprehensive review on Bi_2Te_3-based thin films: Thermoelectrics and beyond. *Interdiscip. Mater.* **2022**, *1* (1), 88−115.
(2) Liu, Z.; Hong, T.; Xu, L.; Wang, S.; Gao, X.; Chang, C.; Ding, X.; Xiao, Y.; Zhao, L.-D. Lattice expansion enables interstitial doping to achieve a high average ZT in n-type PbS. *Interdiscip. Mater.* **2023**, *2* (1), 161−170.
(3) Wu, Z.; Zhang, S.; Liu, Z.; Mu, E.; Hu, Z. Thermoelectric converter: Strategies from materials to device application. *Nano Energy* **2022**, *91*, No. 106692.
(4) Shi, Q.; Li, J.; Zhao, X.; Chen, Y.; Zhang, F.; Zhong, Y.; Ang, R. Comprehensive Insight into p-Type Bi_2Te_3-Based Thermoelectrics near Room Temperature. *ACS Appl. Mater. Interfaces* **2022**, *14* (44), 49425−49445.
(5) Tan, G.; Zhao, L.-D.; Kanatzidis, M. G. Rationally Designing High-Performance Bulk Thermoelectric Materials. *Chem. Rev.* **2016**, *116* (19), 12123−12149.
(6) Snyder, G. J.; Snyder, A. H.; Wood, M.; Gurunathan, R.; Snyder, B. H.; Niu, C. Weighted Mobility. *Adv. Mater.* **2020**, *32* (25), No. 2001537.
(7) Chen, Z.; Zhang, X.; Pei, Y. Manipulation of Phonon Transport in Thermoelectrics. *Adv. Mater.* **2018**, *30* (17), No. 1705617.
(8) Qin, G.; Qin, Z.; Fang, W.-Z.; Zhang, L.-C.; Yue, S.-Y.; Yan, Q.-B.; Hu, M.; Su, G. Diverse anisotropy of phonon transport in two-dimensional group IV−VI compounds: A comparative study. *Nanoscale* **2016**, *8* (21), 11306−11319.
(9) Shafique, A.; Shin, Y.-H. Thermoelectric and phonon transport properties of two-dimensional IV−VI compounds. *Sci. Rep.* **2017**, *7* (1), 506.
(10) Xie, W.; Tang, X.; Yan, Y.; Zhang, Q.; Tritt, T. M. High thermoelectric performance BiSbTe alloy with unique low-dimensional structure. *J. Appl. Phys.* **2009**, *105* (11), No. 113713.
(11) Yang, G.; Sang, L.; Yun, F. F.; Mitchell, D. R. G.; Casillas, G.; Ye, N.; See, K.; Pei, J.; Wang, X.; Li, J.-F.; Snyder, G. J.; Wang, X. Significant Enhancement of Thermoelectric Figure of Merit in BiSbTe-Based Composites by Incorporating Carbon Microfiber. *Adv. Funct. Mater.* **2021**, *31* (15), No. 2008851.
(12) Kumar, S.; Schwingenschlögl, U. Lattice thermal conductivity in layered BiCuSeO. *Phys. Chem. Chem. Phys.* **2016**, *18* (28), 19158−19164.
(13) Zhang, X.; Chang, C.; Zhou, Y.; Zhao, L.-D. BiCuSeO Thermoelectrics: An Update on Recent Progress and Perspective. *Materials* **2017**, *10* (2), 198.
(14) Feng, D.; Zheng, F.; Wu, D.; Wu, M.; Li, W.; Huang, L.; Zhao, L.-D.; He, J. Investigation into the extremely low thermal conductivity in Ba heavily doped BiCuSeO. *Nano Energy* **2016**, *27*, 167−174.
(15) Zhao, L.-D.; Lo, S.-H.; Zhang, Y.; Sun, H.; Tan, G.; Uher, C.; Wolverton, C.; Dravid, V. P.; Kanatzidis, M. G. Ultralow thermal conductivity and high thermoelectric figure of merit in SnSe crystals. *Nature* **2014**, *508* (7496), 373−377.
(16) Chang, C.; Wu, M.; He, D.; Pei, Y.; Wu, C.-F.; Wu, X.; Yu, H.; Zhu, F.; Wang, K.; Chen, Y.; Huang, L.; Li, J.-F.; He, J.; Zhao, L.-D. 3D charge and 2D phonon transports leading to high out-of-plane ZT in n-type SnSe crystals. *Science* **2018**, *360* (6390), 778−783.
(17) Zhu, H.; Zhao, C.; Nan, P.; Jiang, X.-m.; Zhao, J.; Ge, B.; Xiao, C.; Xie, Y. Intrinsically Low Lattice Thermal Conductivity in Natural Superlattice $(Bi_2)_m(Bi_2Te_3)_n$ Thermoelectric Materials. *Chem. Mater.* **2021**, *33* (4), 1140−1148.
(18) Samanta, M.; Biswas, K. 2D Nanosheets of Topological Quantum Materials from Homologous $(Bi_2)_m(Bi_2Se_3)_n$ Heterostructures: Synthesis and Ultralow Thermal Conductivity. *Chem. Mater.* **2020**, *32* (20), 8819−8826.
(19) Ng, H. K.; Xiang, D.; Suwardi, A.; Hu, G.; Yang, K.; Zhao, Y.; Liu, T.; Cao, Z.; Liu, H.; Li, S.; Cao, J.; Zhu, Q.; Dong, Z.; Tan, C. K. I.; Chi, D.; Qiu, C.-W.; Hippalgaonkar, K.; Eda, G.; Yang, M.; Wu, J. Improving carrier mobility in two-dimensional semiconductors with rippled materials. *Nat. Electron.* **2022**, *5* (8), 489−496.
(20) Gao, Z.; Zhu, T.; Sun, K.; Wang, J.-S. Highly Anisotropic Thermoelectric Properties of Two-Dimensional As_2Te_3. *ACS Appl. Electron. Mater.* **2021**, *3* (4), 1610−1620.
(21) Su, L.; Wang, D.; Wang, S.; Qin, B.; Wang, Y.; Qin, Y.; Jin, Y.; Chang, C.; Zhao, L.-D. High thermoelectric performance realized through manipulating layered phonon-electron decoupling. *Science* **2022**, *375* (6587), 1385−1389.
(22) Zhou, Z.; Guo, J.; Zheng, Y.; Yang, Y.; Yang, B.; Li, D.; Zhang, W.; Wei, B.; Liu, C.; Lan, J.-L.; Nan, C.-W.; Lin, Y.-H. Boosting Thermoelectric Performance via Weakening Carrier-Phonon Coupling in BiCuSeO-Graphene Composites. *Small Methods* **2024**, No. 2301619.
(23) Hao, S.; Shi, F.; Dravid, V. P.; Kanatzidis, M. G.; Wolverton, C. Computational Prediction of High Thermoelectric Performance in Hole Doped Layered GeSe. *Chem. Mater.* **2016**, *28* (9), 3218−3226.
(24) Zhang, X.; Shen, J.; Lin, S.; Li, J.; Chen, Z.; Li, W.; Pei, Y. Thermoelectric properties of GeSe. *J. Materiomics* **2016**, *2* (4), 331−337.
(25) Shaabani, L.; Aminorroaya-Yamini, S.; Byrnes, J.; Akbar Nezhad, A.; Blake, G. R. Thermoelectric Performance of Na-Doped GeSe. *ACS Omega* **2017**, *2* (12), 9192−9198.
(26) Sidharth, D.; Alagar Nedunchezhian, A. S.; Akilan, R.; Srivastava, A.; Srinivasan, B.; Immanuel, P.; Rajkumar, R.; Yalini Devi, N.; Arivanandhan, M.; Liu, C.-J.; Anbalagan, G.; Shankar, R.; Jayavel, R. Enhanced thermoelectric performance of band structure engineered $GeSe_{1-x}Te_x$ alloys. *Sustainable Energy Fuels* **2021**, *5* (6), 1734−1746.
(27) Lyu, T.; Li, X.; Yang, Q.; Cheng, J.; Zhang, Y.; Zhang, C.; Liu, F.; Li, J.; Ao, W.; Xie, H.; Hu, L. Stepwise Ge vacancy manipulation enhances the thermoelectric performance of cubic GeSe. *Chem. Eng. J.* **2022**, *442*, No. 136332.
(28) Roychowdhury, S.; Ghosh, T.; Arora, R.; Waghmare, U. V.; Biswas, K. Stabilizing n-Type Cubic GeSe by Entropy-Driven Alloying of $AgBiSe_2$: Ultralow Thermal Conductivity and Promising Thermoelectric Performance. *Angew. Chem., Int. Ed.* **2018**, *57* (46), 15167−15171.
(29) Sarkar, D.; Roychowdhury, S.; Arora, R.; Ghosh, T.; Vasdev, A.; Joseph, B.; Sheet, G.; Waghmare, U. V.; Biswas, K. Metavalent Bonding in GeSe Leads to High Thermoelectric Performance. *Angew. Chem., Int. Ed.* **2021**, *60* (18), 10350−10358.
(30) Wang, Z.; Wu, H.; Xi, M.; Zhu, H.; Dai, L.; Xiong, Q.; Wang, G.; Han, G.; Lu, X.; Zhou, X.; Wang, G. Structure-Dependent Thermoelectric Properties of $GeSe_{1-x}Te_x$ ($0 \le x \le 0.5$). *ACS Appl. Mater. Interfaces* **2020**, *12* (37), 41381−41389.
(31) Yan, M.; Geng, H.; Jiang, P.; Bao, X. Glass-like electronic and thermal transport in crystalline cubic germanium selenide. *J. Energy Chem.* **2020**, *45*, 83−90.
(32) Huang, Z.; Miller, S. A.; Ge, B.; Yan, M.; Anand, S.; Wu, T.; Nan, P.; Zhu, Y.; Zhuang, W.; Snyder, G. J.; Jiang, P.; Bao, X. High Thermoelectric Performance of New Rhombohedral Phase of GeSe stabilized through Alloying with $AgSbSe_2$. *Angew. Chem., Int. Ed.* **2017**, *56* (45), 14113−14118.
(33) Yan, M.; Tan, X.; Huang, Z.; Liu, G.; Jiang, P.; Bao, X. Synergetic optimization of electronic and thermal transport for high-performance thermoelectric GeSe−$AgSbTe_2$ alloy. *J. Mater. Chem. A* **2018**, *6* (18), 8215−8220.
(34) Sarkar, D.; Ghosh, T.; Roychowdhury, S.; Arora, R.; Sajan, S.; Sheet, G.; Waghmare, U. V.; Biswas, K. Ferroelectric Instability

Induced Ultralow Thermal Conductivity and High Thermoelectric Performance in Rhombohedral p-Type GeSe Crystal. *J. Am. Chem. Soc.* **2020**, *142* (28), 12237−12244.
(35) Huang, Y.; Lyu, T.; Zeng, M.; Wang, M.; Yu, Y.; Zhang, C.; Liu, F.; Hong, M.; Hu, L. Manipulation of metavalent bonding to stabilize metastable phase: A strategy for enhancing *zT* in GeSe. *Interdiscip. Mater.* **2024**, No. e12170.
(36) Guo, M.; Cui, H.-H.; Guo, W.; Chen, Z.; Ming, H.; Luo, Z.-Z.; Zou, Z. Achieving Superior Thermoelectric Performance in Ge_4Se_3Te via Symmetry Manipulation with I−V−VI_2 Alloying. *Adv. Funct. Mater.* **2024**, *34* (18), No. 2313720.
(37) Li, X.; Liang, Z.; Li, J.; Cheng, F.; He, J.; Zhang, C.; Li, J.; Liu, F.; Lyu, T.; Ge, B.; Hu, L. Crystal symmetry enables high thermoelectric performance of rhombohedral GeSe($MnCdTe_2$). *Nano Energy* **2022**, *100*, No. 107434.
(38) Muir, J. A.; Beato, V. Phase transformations in the system GeSe−GeTe. *J. Less-Common Met.* **1973**, *33* (3), 333−340.
(39) Wiedemeier, H.; Siemers, P. A. The Temperature−Composition Phase Diagram of the GeSe−GeTe System. In *Modern High Temperature Science: A Collection of Research Papers from Scientists, Post-Doctoral Associates, and Colleagues of Professor Leo Brewer in Celebration of His 65th Birthday*; Margrave, J. L., Ed.; Humana Press: Totowa, NJ, 1984; pp 395−408, DOI: 10.1007/978-1-4612-5180-4_23.
(40) García-Lastra, J. M.; García-Fernández, P.; Calle-Vallejo, F.; Trueba, A.; Aramburu, J. A.; Moreno, M. Quantifying Local and Cooperative Components in the Ferroelectric Distortion of $BaTiO_3$: Learning from the Off-Center Motion in the $MnCl_6^{5-}$ Complex Formed in KCl:Mn^+. *Inorg. Chem.* **2014**, *53* (13), 6534−6543.
(41) Arshad, M.; Khan, W.; Rajput, P.; Kumar, M.; Abushad, M.; Husain, S. Synchrotron based X-ray absorption spectroscopy investigation and temperature dependent ferroelectric properties of Ni doped $BaTiO_3$ nanostructures. *Ceram. Int.* **2022**, *48* (10), 14156−14165.
(42) Luo, Z.-Z.; Cai, S.; Hao, S.; Bailey, T. P.; Su, X.; Spanopoulos, I.; Hadar, I.; Tan, G.; Luo, Y.; Xu, J.; Uher, C.; Wolverton, C.; Dravid, V. P.; Yan, Q.; Kanatzidis, M. G. High Figure of Merit in Gallium-Doped Nanostructured n-Type PbTe-*x*GeTe with Midgap States. *J. Am. Chem. Soc.* **2019**, *141* (40), 16169−16177.
(43) Yang, X.; Li, X.-M.; Li, Y.; Li, Y.; Sun, R.; Liu, J.-N.; Bai, X.; Li, N.; Xie, Z.-K.; Su, L.; Gong, Z.-Z.; Zhang, X.-Q.; He, W.; Cheng, Z. Three-Dimensional Limit of Bulk Rashba Effect in Ferroelectric Semiconductor GeTe. *Nano Lett.* **2021**, *21* (1), 77−83.
(44) Perdew, J. P.; Burke, K.; Ernzerhof, M. Generalized Gradient Approximation Made Simple. *Phys. Rev. Lett.* **1996**, *77* (18), 3865−3868.
(45) Kresse, G.; Furthmüller, J. Efficient iterative schemes for ab initio total-energy calculations using a plane-wave basis set. *Phys. Rev. B* **1996**, *54* (16), 11169−11186.
(46) Yu, Y.; Zhou, C.; Ghosh, T.; Schön, C.-F.; Zhou, Y.; Wahl, S.; Raghuwanshi, M.; Kerres, P.; Bellin, C.; Shukla, A.; Cojocaru-Mirédin, O.; Wuttig, M. Doping by Design: Enhanced Thermoelectric Performance of GeSe Alloys Through Metavalent Bonding. *Adv. Mater.* **2023**, *35* (19), No. 2300893.
(47) Yao, W.; Zhang, Y.; Lyu, T.; Huang, W.; Huang, N.; Li, X.; Zhang, C.; Liu, F.; Wuttig, M.; Yu, Y.; Hong, M.; Hu, L. Two-step phase manipulation by tailoring chemical bonds results in high-performance GeSe thermoelectrics. *Innovation* **2023**, *4* (6), No. 100522.
(48) Cutler, M.; Leavy, J.; Fitzpatrick, R. Electronic transport in semimetallic cerium sulfide. *Phys. Rev.* **1964**, *133* (4A), A1143.
(49) Lin, F.-H.; Liu, C.-J. An algorithm of calculating transport parameters of thermoelectric materials using single Kane band model with Riemann integral methods. *Sci. Rep.* **2022**, *12* (1), 7056.
(50) Hu, L.; Duan, B.; Lyu, T.; Lin, N.; Zhang, C.; Liu, F.; Li, J.; Wuttig, M.; Yu, Y. In Situ Design of High-Performance Dual-Phase GeSe Thermoelectrics by Tailoring Chemical Bonds. *Adv. Funct. Mater.* **2023**, *33* (17), No. 2214854.
(51) Qin, B.; He, W.; Zhao, L.-D. Estimation of the potential performance in p-type SnSe crystals through evaluating weighted mobility and effective mass. *J. Materiomics* **2020**, *6* (4), 671−676.
(52) Guo, R.; Wang, X.; Kuang, Y.; Huang, B. First-principles study of anisotropic thermoelectric transport properties of IV-VI semiconductor compounds SnSe and SnS. *Phys. Rev. B* **2015**, *92* (11), No. 115202.
(53) Kim, H.; Kaviany, M. Effect of thermal disorder on high figure of merit in PbTe. *Phys. Rev. B* **2012**, *86* (4), No. 045213.
(54) Li, W.; Carrete, J.; Madsen, G. K. H.; Mingo, N. Influence of the optical-acoustic phonon hybridization on phonon scattering and thermal conductivity. *Phys. Rev. B* **2016**, *93* (20), No. 205203.
(55) Sajjad, M.; Singh, N. Interlayer Coupling Induced Phonon-Glass−Electron-Crystal Behavior in van der Waals Heterostructure $PtSe_2$/γ-GeSe. *ACS Appl. Energy Mater.* **2022**, *5* (11), 13610−13616.
(56) Juneja, R.; Singh, A. K. Rattling-induced ultralow thermal conductivity leading to exceptional thermoelectric performance in $AgIn_5S_8$. *ACS Appl. Mater. Interfaces* **2019**, *11* (37), 33894−33900.
(57) Degueldre, C.; Tissot, P.; Lartigue, H.; Pouchon, M. Specific heat capacity and Debye temperature of zirconia and its solid solution. *Thermochim. Acta* **2003**, *403* (2), 267−273.
(58) Phillips, N. E. Low-temperature heat capacity of metals. *CRC Crit. Rev. Solid State Sci.* **1971**, *2* (4), 467−553.
(59) Lin, H.; Tan, G.; Shen, J.-N.; Hao, S.; Wu, L.-M.; Calta, N.; Malliakas, C.; Wang, S.; Uher, C.; Wolverton, C.; Kanatzidis, M. G. Concerted rattling in $CsAg_5Te_3$ leading to ultralow thermal conductivity and high thermoelectric performance. *Angew. Chem., Int. Ed.* **2016**, *55* (38), 11431−11436.
(60) Ying, P.; Li, X.; Wang, Y.; Yang, J.; Fu, C.; Zhang, W.; Zhao, X.; Zhu, T. Hierarchical Chemical Bonds Contributing to the Intrinsically Low Thermal Conductivity in α-MgAgSb Thermoelectric Materials. *Adv. Funct. Mater.* **2017**, *27* (1), No. 1604145.
(61) Xie, H.; Su, X.; Zhang, X.; Hao, S.; Bailey, T. P.; Stoumpos, C. C.; Douvalis, A. P.; Hu, X.; Wolverton, C.; Dravid, V. P.; Uher, C.; Tang, X.; Kanatzidis, M. G. Origin of Intrinsically Low Thermal Conductivity in Talnakhite $Cu_{17.6}Fe_{17.6}S_{32}$ Thermoelectric Material: Correlations between Lattice Dynamics and Thermal Transport. *J. Am. Chem. Soc.* **2019**, *141* (27), 10905−10914.
(62) Grigera, T.; Martin-Mayor, V.; Parisi, G.; Verrocchio, P. Vibrational spectrum of topologically disordered systems. *Phys. Rev. Lett.* **2001**, *87* (8), No. 085502.
(63) Su, X.; Zhao, N.; Hao, S.; Stoumpos, C. C.; Liu, M.; Chen, H.; Xie, H.; Zhang, Q.; Wolverton, C.; Tang, X.; Kanatzidis, M. G. High Thermoelectric Performance in the Wide Band-Gap $AgGa_{1-x}Te_2$ Compounds: Directional Negative Thermal Expansion and Intrinsically Low Thermal Conductivity. *Adv. Funct. Mater.* **2019**, *29* (6), No. 1806534.